Article

0D Bismuth(III)-Based Hybrid Ferroelectric: Tris(acetamidinium) Hexabromobismuthate(III)

Klaudia Mencel, Vasyl Kinzhybalo, Ryszard Jakubas, Jan K. Zaręba, Przemysław Szklarz, Piotr Durlak, Marek Drozd, and Anna Piecha-Bisiorek*

Read Online

ACCESS | Metrics & More | Article Recommendations | Supporting Information

ABSTRACT: Ferroelectric properties of haloantimonates(III) and halobismuthates(III) have been detected for as much as 40 structures belonging to 7 different types of anionic networks, with RMX_4, R_2MX_5, $R_3M_2X_9$, and $R_5M_2X_{11}$ stoichiometries being the most frequently reported to host these properties. We report on the first ferroelectric of the halobismuthate(III) family with a R_3MX_6 stoichiometry, that is, tris(acetamidinium)hexabromobismuthate(III), $(CH_3C-(NH_2)_2)_3[BiBr_6]$ (**ABB**), characterized by a one-component organic network. While the stoichiometry and crystal packing of **ABB** might seem uncomplicated, the temperature-resolved structural and spectroscopic studies paint a different picture in which rich polymorphism in the solid state occurs between tetragonal (paraelastic) and triclinic (ferroelastic) crystal phases: **I** ($P4_2/n$) → **II** ($P\bar{1}$) at 272/277 K (cooling/heating), **II** ($P\bar{1}$) → **III** ($P\bar{1}$) at 207 K, and **III** ($P\bar{1}$) → **IV** ($P1$) at 98/127 K. The ferroelectric properties of phase **IV** have been confirmed by the pyroelectric current and hysteresis loop measurements; additionally, the acentric symmetry has been further supported by second harmonic generation measurements. Crystallographic analysis of phase **III** reveals the antiparallel alignment of acetamidinium dipoles, pointing to the antiferrroelectric nature of this phase. In turn, the character of the ferroelectric transition (**III** → **IV**) should be considered as "displacive" for both cationic and anionic substructures.) In this report, we also explore the two-photon absorption property of **ABB** at 800 nm, a property that is unexplored for any halobismuthate(III) thus far. We also present periodic ab initio calculations for **ABB** crystals. The Berry-phase approach at the Hartree−Fock and density functional theory (DFT-D3) method levels is employed for spontaneous polarization calculations. The origin of ferroelectric polarization is studied using DFT-D3 and RHF electronic structure calculations, emphasizing the relationship between P_s and the relative orientation of organic/inorganic components.
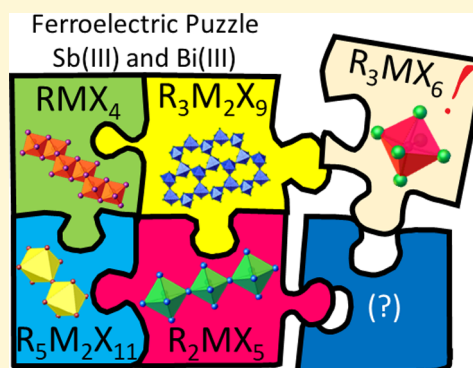
1. INTRODUCTION

Hybrid materials with a rich solid-to-solid phase transition (PT) behavior attract widespread attention because of their high-profile applications in which they could be employed. A special place in this group of compounds is occupied by organic−inorganic hybrids based on divalent and trivalent metal halides whose temperature-dependent electrical and optical properties are relevant for emerging applications (e.g., photovoltaics, dielectrics, ferroelectrics, and nonlinear optical (NLO) switches).[1−5]

Molecular-ionic salts based on haloantimonates(III) and halobismuthates(III), described by the general formula $R_aM_bX_{3b+a}$ (where R stands for an organic cation, M = Sb(III) or Bi(III), and X = Cl, Br, and I), have become a focus of interest as many members of this family reveal ferroelectric and/or ferroelastic properties (ferroic materials).[6] A large body of experimental data have shown that the anionic subnetwork can accommodate various compositions of the first coordination sphere; thus, to date, more than 40 different anionic forms based on the $[MX_6]^{3-}$ generic unit have been known.[7] An

additional degree of chemical freedom is due to the possibility of manipulating the connectivity modes between octahedral units (i.e., via corners, edges, or faces) which, in turn, dictates whether isolated forms, infinite one-dimensional (1D) chains, two-dimensional (2D) layers, or three-dimensional (3D) networks are formed. One should note, however, that in this particular subgroup, ferroelectric ordering is not a general feature but is limited only to specific stoichiometries, that is, $R_3M_2X_9$ [the inorganic part is built up of 2D layers or isolated units (0D)], $R_5M_2X_{11}$ (isolated bioctahedra), R_2MX_5 (1D chains of different configurations), and RMX_4 (1D chains).[6,7]

Haloantimonate(III) and halobismuthate(III) materials comprising isolated/discrete $[MX_6]^{3-}$ moieties are quite
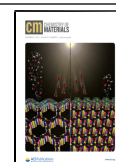
common, yet their PT behavior in a wide temperature range remains largely unknown. Generally, the crystal structure may be complex due to the excess of organic cations and solvent molecules (mainly water), thus the general formula may be described as follows: $R_3MX_6 \cdot (RX)_n \cdot xH_2O$ (n = 1−3, x = 1−2). It is worth noting that this type of connection occurs regardless of the size and symmetry of the cation, as well as the type of halogen ion. The first compound from this subclass, $(NH_2(CH_3)_2)_3[BiBr_6]$ (R = dimethylammonium), was structurally characterized in 1968 by McPherson and Meyers.[8] Despite the extensive on-going research on haloantimonates-(III) and halobismuthates(III) since the 1970s, the knowledge concerning the physical properties of R_3MX_6-type compounds (n, x = 0) is fragmentary so far. Of a total of about 270 compounds, 42 of them crystallize in acentric groups, and only a handful of them adopt polar space groups. Some of the most interesting examples are the dialkylammonium derivatives crystallizing in the polar space group $R3c$[9,10] and allylammonium analogues characterized by a complex sequence of PTs and ferroelastic properties.[11,12] Within the R_3MX_6 subgroup, above-room-temperature (RT) switching of the second harmonic generation (SHG) response has been reported for $(C_4H_{16}N_3)[BiBr_6]$ by Wu[13] and visible luminescence for $(C_6H_5-CH_2NH_3)_3[MBr_6]$ (M = Bi(III) and Sb(III)) by Chen.[14]

Recently, the first mononuclear halobismuthate(III) comprising two disparate organic cations has been reported by Wang et al.[15] Indeed, in this case, the cationic substructure consists of two different moieties: one dimethylammonium (R′) and two benzylammonium (R″) cations, whereas the anionic component consists of an isolated octahedral unit $[BiBr_6]^{3-}$. $[((CH_3)_2NH_2)(C_6H_5CH_2NH_2)_2][BiBr_6]$ appears to be a RT multiaxial ferroelectric with P_s = 1.0 μC·cm^{-2}. The molecular mechanism of the ferroelectric PT is attributed to the change in the dynamics of the organic cations, and, for this reason, the transition was classified as an "order−disorder" type. The discovery of a new type of halobismuthate(III) connection with mixed cationic substructures creates a new path, which enables the design of molecular multiaxial ferroelectrics.

In light of the above-presented outcomes, it seems interesting to extend the research on the group of haloantimonates(III) and halobismuthates(III) in this particular chemical stoichiometry (R_3MX_6). Successfully, we have synthesized a unique, multiferroic (ferroelectric and ferroelastic) compound: tris(acetamidinium) hexabromobismuthate-(III) $(CH_3C(NH_2)_2)_3[BiBr_6]$ (hereafter abbreviated as **ABB**). Its structural and physicochemical properties were explored in detail, revealing the molecular origin of reversible spontaneous polarization (P_s) below 127 K. Noteworthily, **ABB** is the first example of a "pure" organic−inorganic hybrid ferroelectric within halobismuthates(III) of the R_3MX_6 type of stoichiometry characterized by a one-component organic network. Experimental characterizations of **ABB**, focused primarily on the polar order of its lowest temperature phase, are further supported by periodic ab initio calculations of P_s by employing the Berry-phase (BP) approach at the Hartree−Fock (HF) and density functional theory (DFT-D3) method levels.

2. EXPERIMENTAL SECTION

2.1. Synthesis. For the synthesis of $(CH_3C(NH_2)_2)_3[BiBr_6]$ (**ABB**), acetamidinium bromide is needed. This compound is not commercially available, therefore we obtained acetamidinium bromide

by 3-fold recrystallization from a solution of acetamidinium chloride (Sigma-Aldrich, 95%) in concentrated HBr (Sigma-Aldrich, 48%). Crystals of **ABB** obtained in the form of yellow longitudinal plates (Figure S1) were reacted with stoichiometric amounts of acetamidinum bromide and bismuth(III) oxide (Sigma-Aldrich, 99.99%) with the addition of HBr in a methanol solution. The crystals were grown by the slow evaporation at constant room temperature. The chemical composition was verified by an elemental analysis: C: 2.15% (theor. 2.13%), N: 4.98% (theor. 4.96%), and H: 1.05% (theor. 1.01%). The phase purity of the **ABB** was verified using powder X-ray diffraction (see Figure S2).

2.2. Thermal Properties. Differential scanning calorimetry (DSC) experiments were carried out using a Metler Toledo DSC3 (300−160 K) and PerkinElmer (160−95 K) differential scanning calorimeters, which were calibrated using n-heptane and indium. DSC measurements were performed under a nitrogen atmosphere, and the monocrystalline material was placed in hermetically sealed Al pans.

Thermogravimetric analysis (TGA) and differential thermal analysis (DTA) were simultaneously performed using a Setaram SETSYS 16/18 instrument in the 300−650 K range with a ramp rate of 5 K·min^{-1} (Figure S3). The scans were carried out under a flow of nitrogen (flow rate: 1 dm^3·h^{-1}).

2.3. Optical Measurements. The ferroelastic domain structures of the **ABB** crystals were observed by means of an Olympus BX53 optical polarization microscope combined with a LINKAM THM-600 heating/cooling stage. The temperature was stabilized to within 0.1 K.

2.4. Dielectric Studies. The complex dielectric permittivity, $\varepsilon^* = \varepsilon' - i\varepsilon''$, was measured between 80 and 300 K using an Agilent E4980A precision LCR meter in the frequency range of an 135 Hz−2 MHz. The overall experimental uncertainties were less than 5%. The dielectric experiment was performed on the single crystal and polycrystalline samples in the form of pressed pellets with geometrical parameters (S = 20−25 mm^2, d = 0.5−0.8 mm). The dimensions of the crystal were 5 mm × 3 mm × 0.8 mm. The silver electrodes were painted on both opposing faces.

The pyroelectric measurement was carried out by using an electrometer/high-resistance meter Keithley 6517B with a temperature ramp of 2 K·min^{-1} (the temperature range: 80−300 K). This measurement was carried out on a pellet sample.

The ferroelectric hysteresis loop measurements were carried out using a modified Sawyer−Tower circuit Precision Premier II (Radiant Technologies, Inc.) at a frequency of 50 Hz (pellet sample). All dielectric studies were performed in a controlled atmosphere (N_2).

2.5. Single-Crystal X-ray Diffraction Analysis. The X-ray diffraction (XRD) data were collected on an Oxford Diffraction Xcalibur four-circle diffractometer equipped with an Atlas CCD camera and a cryocooler device. The data were collected using Mo Kα radiation on heating at 100, 150, 240, and 295 K (more information in the Supporting Information, Table S1). The data reductions were carried out with the use of CrysAlisPro.[16] The structure solution and refinement were carried out with the use of SHELXT.[17] Low-temperature diffraction data reveal extensive twinning of the crystal, which is the result of the domain structure that appears on transition from the tetrahedral RT phase to LT triclinic phases. Diffraction data for the phases **II**, **III**, and **IV** were reduced as four-component twins and refined with the use of the HKLF 5 type reflection file (a 0.319(3):0.323(2):0.1777(15):0.1806(15) ratio in phase **II**, a 0.310(3):0.339(2):0.1709(16):0.1801(16) ratio in phase **III**, and a 0.314(4):0.318(3):0.181(2):0.187(2) ratio in phase **IV**). Details of the structure refinement are included in the deposited cif (nos: 2076562−2076565) and in the Supporting Information.

The powder diffraction pattern for the studied material was collected in Bragg−Brentano geometry at room temperature on a PANalytical X'Pert Pro diffractometer using Cu Kα radiation and compared with the theoretical pattern simulated from the phase **I** single-crystal data (Figure S2).

2.6. Computational Methods (Periodic Ab Initio Calculations). A series of full geometry, cell optimizations, and P_s calculations were performed to localize the key stationary points on the potential energy surface (PES) of the **ABB** in the solid state.

These calculations employed the London-type empirical correction in the (D3) variant for dispersion interactions as proposed by Grimme[18−21] including three-body dispersion contributions with fast analytical gradients together with the vibrational harmonic frequency calculations. The structural data (starting geometry) were taken from the X-ray crystal structure of **ABB** in phase **IV**. Calculations were performed using the CRYSTAL17 software,[22,23] utilizing the two different quantum methods, that is, restricted HF (RHF) and DFT-D3 methods with the hybrid functional: the Becke's three-parameter functional combined with the nonlocal correlation Lee−Yang−Parr (B3LYP-D3)[19,24−26] with the two shrinking factors 4′4′ to generate a commensurate grid of k-points in reciprocal space, following the Monkhorst−Pack[27] net method. Calculations were carried out with the Karlsruhe basis set def2-SVP (split valence polarization) as proposed by Ahlrichs[28,29] and co-workers. Only for the bismuth atom, Hay and Wadt[30−32] large-core effective core pseudopotential has been used. To check if the crystal structure of **ABB** is at the global minimum on the PES after optimization, IR harmonic frequencies were calculated. The imaginary frequencies were not found. For the **ABB** crystal, vibrational frequency calculations using CRYSTAL17 were performed at the Γ-point.[33,34]

2.7. Nonlinear Optical Measurements. Investigations of NLO properties of **ABB** were performed using a QUANTRONIX Integra-C regenerative amplifier operating at 800 nm wavelength. This instrument delivers laser pulses of ∼130 fs duration, and operates at a repetition rate of 1 kHz with an average power up to 1 W. Prior to measurements, the single crystals of **ABB** were crushed with a spatula and sieved through a minisieve set (Sigma-Aldrich), achieving microcrystals with a size of 88−125 μm. The laser beam was directed onto samples at 45°, and was unfocused in all cases. Signal-collecting optics, mounted to the glass optical fiber, was placed perpendicularly to the plane of the sample (backscattering geometry). Scattered pumping radiation was suppressed with the use of a 700 nm shortpass dielectric filter (FESH0700, Thorlabs). Attenuation of laser beam intensity was performed with the use of a round reflective mirror (Thorlabs). All emission spectra were recorded using an Ocean Optics QE Pro-FL spectrograph. Temperature-resolved SHG (TR-SHG) (from 78 to 293 K) was conducted using a 800 nm beam of a 820 mW average power. Temperature control of the single-crystal sample was performed using the Linkam LTS420 heating/freezing stage. The spectra were collected for 2000 ms at each temperature point. Power-dependent measurements were performed by plotting the emission spectra of **ABB** obtained under 800 nm excitation as a function of different laser powers (108−277 mW).

Determination of the two-photon brightness value at 800 nm was performed with the use of the solid-state two-photon exited fluorescence (SSTPEF) technique. The average intensity of the used beam was equal to 310 mW. Prior to SSTPEF measurements, the solid samples of **ABB** and reference compound bis(4-diphenylamino)stilbene (BDPAS) were finely crushed and fixed between microscope glass slides. The two-photon excited emissions of **ABB** and BDPAS were collected using exactly the same beam and geometrical parameters. The density of **ABB** (2.52 g·cm⁻³), necessary for the calculation of the two-photon brightness value, was taken from the crystallographic data for the room-temperature phase.

3. RESULTS AND DISCUSSION

3.1. Thermal Analysis. The overall picture of **ABB** phase behavior includes three reversible PTs of different nature (discontinuous and continuous ones) below RT. As is presented in Figure 1, the first one, at 272/277 K (cooling/heating), is a well-shaped thermal anomaly, while the remaining two, at 207 and 98/127 K, are barely noticeable on DSC curves. The discontinuous nature of the PT between phases **I** and **II** is obvious, and the associated value of the entropy change (ΔS = 9.4 J·mol⁻¹·K⁻¹) indicates its "order−disorder" molecular mechanism. If one considers the PT **II** → **III**, a continuous nature of this structural transformation is
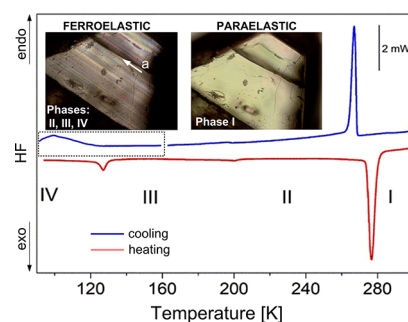

Figure 1. DSC curves of the **ABB** sample [m = 0.01045 g, rate 10 K min⁻¹ (Mettler Toledo DSC3)]. The cooling cycle between 160 and 95 K (dotted frame) was performed using a PerkinElmer instrument (m = 0.04275 g, rate 10 K min⁻¹).

postulated (small-temperature hysteresis), whereas the transition **III** → **IV** features a primarily discontinuous character, albeit there are signatures of a concomitant second-order PT behavior, manifested, for example, in the TR-SHG results (vide infra). The **ABB** sample is stable up to about 420 K (see Figure S3) and does not show any signs of PT in a high-temperature range.

3.2. X-ray Structure Analysis. The **ABB** compound crystallizes in a tetragonal space group type ($P4_2/n$) at room temperature. The independent part of the unit cell (phase **I**, Figure 2a) consists of one $[\text{BiBr}_6]^{3−}$ octahedron and four acetamidinium cations [two of them with 100% occupation (A and B), whereas another two with 50% occupation factors (C and D)]. The independent part possesses a pseudoinversion center at the center of the octahedron. The octahedron lies in the general position at ∼(1/2, 1/4, 1/2), and is surrounded by eight hydrogens bonded to its acetamidinium cations (three A, three B, one C, and one D). The distortion of the octahedron is quite small: Bi−Br distances are in the 2.8265(11)−2.8739(11) Å range, whereas the Br−Bi−Br angles are in the ranges 87.56(3)−92.50(4) and 178.60(3)−179.75(4)° (Table S2). Every bromine atom is involved in the formation of hydrogen bonds as an acceptor (Table S6). Acetamidinium cations A and B are completely ordered and lie in general positions, while disordered cations C and D lie on four-fold axes, $\overline{4}$ and 4_2, respectively. This results in their disorder over two opposite positions.

Crystal packing viewed along the four-fold axis direction (Figure S4) consists of isolated octahedral $[\text{BiBr}_6]^{3−}$ anions and acetamidinium cations residing in-between octahedra. The cations packed in columns along the four-fold axes are disordered, while the remaining ones are ordered.

PT from phase **I** to phase **II** takes place at 272/277 K, and results in the emergence of a domain structure (inset in Figure 1) as evidenced by optical microscopy studies. Single-crystal XRD studies indicate extensive twinning of the crystal in phase **II**, with at least four types of domains rotated by ∼90 and ∼180° with respect to each other, along the direction of the four-fold axis of phase **I**. During transition from phase **I** to phase **II**, the crystal symmetry decreases from tetragonal to triclinic. The volume of the triclinic cell is around half of the volume of the tetragonal cell due to halving of one of the cell parameters. The independent part of the unit cell in phase **II** consists of one full $[\text{BiBr}_6]^{3−}$ octahedron and two-halves of $[\text{BiBr}_6]^{3−}$ octahedra (lying on centers of inversion), along with six acetamidinium cations, one of which is disordered over two positions [0.66(5):0.34(5)]. Thus, in comparison with
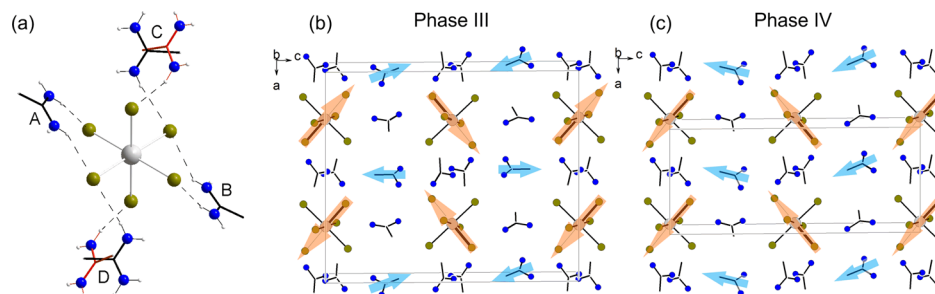
Figure 2. (a) Independent part of the unit cell of **ABB** (phase **I**); (b,c) mutual orientation of the dipole moments of organic (blue) and inorganic (orange) substructures between **III** and **IV**.
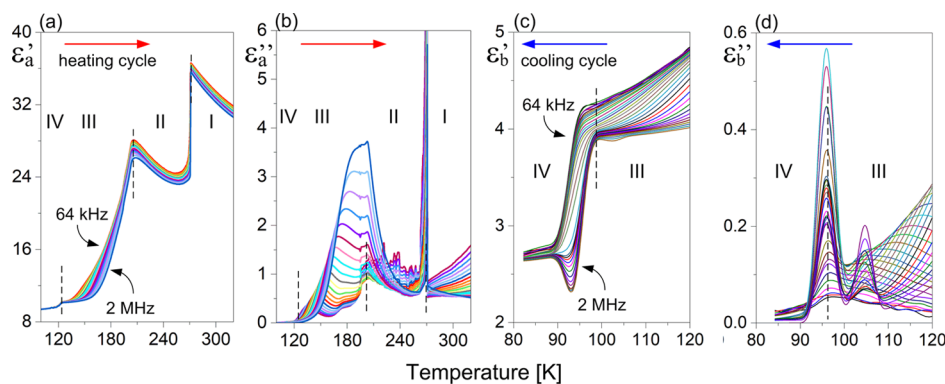

Figure 3. Temperature dependence of the real part of the complex dielectric permittivity $[\varepsilon^* = \varepsilon' - i\varepsilon''$, where ε' is the real (a,c) and ε'' is the imaginary part (b,d)] at selected frequencies between 64 kHz and 2 MHz along the (a,b) a-axis during the heating cycle and (c,d) b-axis during the cooling cycle in the vicinity of ferroelectric transition.

tetragonal phase, one-half of the disordered cations becomes ordered in such a way that in columns every second disordered cation reorients to occupy one position. Interestingly, the $[BiBr_6]^{3-}$ octahedron reveals the axial distortion, that is, one of the Bi−Br bond distances elongates [Bi1A−Br4A 2.932(4) Å] while the opposite shortens [Bi1A−Br2A 2.772(4) Å], whereas the remaining Bi−Br bond distances are in the 2.822(5)− 2.868(4) Å range (Tables S3 and S7).

PT **II** → **III** is evidenced in the XRD pattern by the occurrence of weak superstructure reflections along the direction of the 4-fold axis of the tetragonal phase. The supercell of **III** is doubled with respect to **II** but still takes a triclinic crystal symmetry. Consequently, the contents of the independent part are twice the contents of phase **II**. The crystal structures of **II** and **III** are very similar with the most prominent difference being the ordering of the remaining disordered cations, thus resulting in a completely ordered structure, characterized by the antiparallel orientation of the just-ordered cations (Figure 2b). The cell parameter doubling, weak superstructure reflections, and antiparallel arrangement of cations are indicative of the paraelectric−antiferroelectric nature of **II** → **III** PT (Tables S4 and S8).

During the last PT, that is, **III** → **IV**, the superstructure reflections disappear, and the unit cell of **IV** becomes similar to the one of phase **II**. Crystal symmetry is triclinic, and the structure can be solved in both centrosymmetric $P\bar{1}$ and noncentrosymmetric $P1$ space groups. The structure in $P\bar{1}$ reveals disorder in one of the cation positions, and the structural model is practically identical to that of phase **II**. By contrast, the structure in the $P1$ space group is completely ordered. Because dielectric and TR-SHG studies confirm the ferroelectric character of phase **IV** (vide infra), the non-

centrosymmetric structural model is accepted as correct. The most prominent change that takes place during the **III** → **IV** PT is the reorientation of the cations, which were arranged in an antiparallel fashion in phase **III**, so that their dipole moments are not canceled anymore in phase **IV** (Figure 2c).

Quite interesting structural information can be obtained from the analysis of deformation of $BiBr_6$ octahedra during the PTs. In phase **I**, Bi−Br bond lengths fall within the narrow region of 2.8265(11)−2.8739(11) Å, so it may be considered as symmetrical, meaning nonpolar (Table S2). Already in phase **II**, one of the $BiBr_6$ octahedra becomes deformed. The axial deformation results in shortening of one of the Bi−Br bonds to 2.772(4) Å and elongation of the opposite Bi−Br bond to 2.932(4) Å. Such a deformation results in the emergence of the dipole moment of the $BiBr_6$ octahedron along the axis of deformation (Table S3). In phase **III**, all octahedra become deformed (Table S4), as well as all cations become ordered. Because the structure of phase **III** is centrosymmetric, dipole moments of cations and anions canceled out (Figure 2b). On transition to polar phase **IV**, some of the cations reorient and some of the $BiBr_6$ octahedra change their deformation pattern (Tables S5 and S9), so that their dipole moments are no more counterbalanced (Figure 2c). Taking the above into consideration, the character of **III** → **IV** PT should be considered as "displacive" for both cationic and anionic substructures. On the contrary, during the remaining PTs, the anionic substructure is subject to "displacive" and the cationic substructure to "order−disorder" changes. Such a mixed nature of PTs is consistent with the observations of changes in the dielectric permittivity.

3.3. Dielectric Properties. The temperature behavior of the dielectric function, $\varepsilon'(T, \omega)$ and $\varepsilon''(T, \omega)$, in the
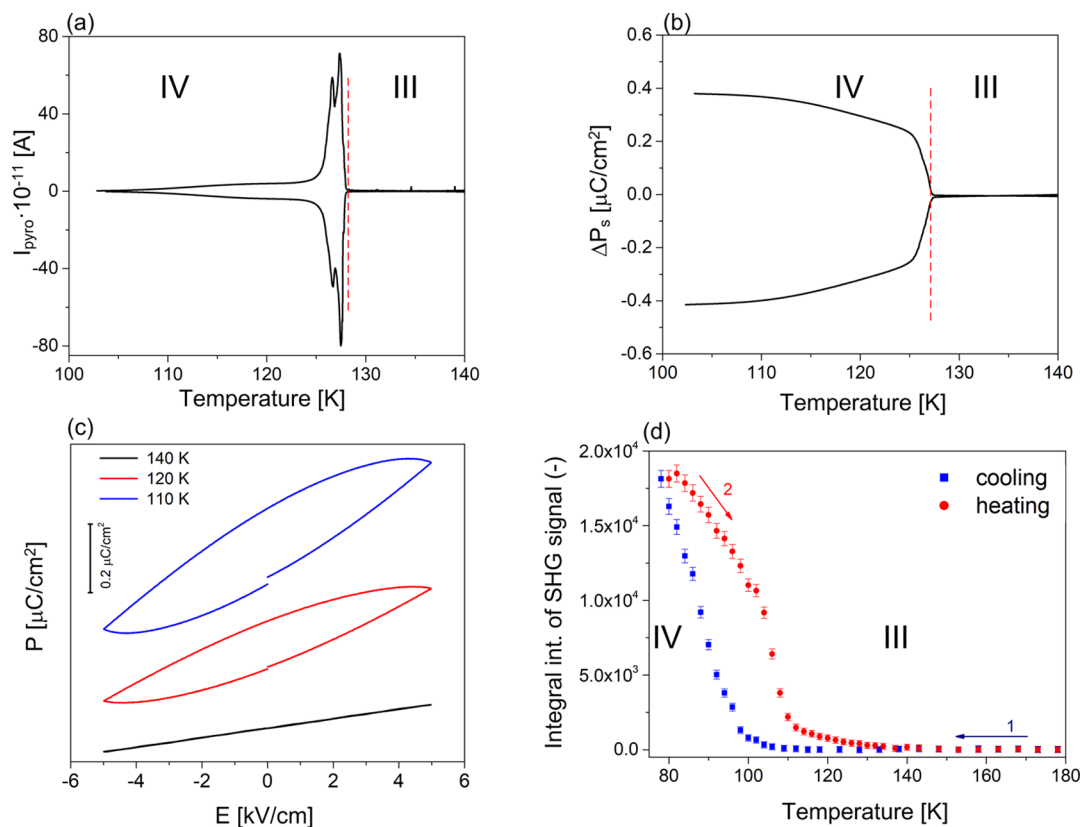
Figure 4. (a) Temperature dependence of the pyroelectric current during heating in the vicinity of antiferroelectric−ferroelectric PT; (b) spontaneous polarization calculated by the integration of the pyroelectric current. (c) P−E hysteresis loops at various temperatures; (d) plots of integral intensities of the SHG signal of **ABB** for cooling (blue squares) and heating (red circles) runs.

temperature range covering three PTs in **ABB** is illustrated in Figure 3a,b. All PTs recorded by DSC measurements are dielectrically active, and indicate distinct anisotropy of these properties. The most spectacular dielectric response (between phases **I−III**) is observed along the *a*-axis (Figure 3a,b), while the ferroelectric PT is almost unnoticeable. By contrast, the dielectric response observed between phases **III−IV** along the *b*-axis (Figure 3c,d) is a well-shaped anomaly. Nevertheless, the sequence of PTs and dielectric response accompanying these transitions seems to be perplexing especially if one takes into account the P_s results. The dielectric anomalies are significant, and the one close to **I → II** PT is characteristic of antiferroelectric transition, whereas those in the vicinity of the **II → III** PT resemble anomalies encountered in typical ferroelectrics. However, based on the X-ray results (doubling of the unit cell volume and the antiparallel arrangement of the acetamidinium dipoles), only the phase **III** may be considered as an antiferroelectric one. Unfortunately, in this case, the external electric field needed to induce a double loop is very high (above 30 kV·cm^{-1}) and the experiment itself requires a specific approach,[35] which we were not able to apply, especially, in the lowest temperature range.

The dielectric anomaly seen as a step-like decrease in ε', accompanying the ferroelectric PT (**III → IV**), suggests that we deal with a so-called weak ferroelectric.[36] Additionally, during this transformation, the number of molecules in the unit cell changes so the P_s cannot be a transition parameter. It follows that the transition in question possesses improper ferroelectric characteristics.[37,38]

In order to confirm the polar properties of **ABB** crystals, the pyroelectric measurements were carried out. The temperature characteristics of the pyroelectric current are shown in Figure 4a. Single crystals of **ABB** were polarized by an external electric field, E_{ext}, as high as ±8 kV cm^{-1} in phase **III**, and then slowly cooled down to phase **IV**. The measurements of I_{pyro} were made during heating run for two opposite polarities. The value of spontaneous polarization (P_s) was estimated from the integration of I_{pyro} over time. The reversed P_s value reached ca. 0.4 μC cm^{-2} 20 K below T_c (Figure 4b), while the P_s value from the P−E loop (Figure 4c) is distinctly smaller (0.1 μC cm^{-2}) than that from the pyroelectric measurements. The differences in these P_s values are linked to the fact that in the P(E) experiment, P_s is unsaturated even at as high electric field as 4.5×10^6 V·m^{-1}. Additionally, over the phases **II**, **III**, and **IV**, the sample of **ABB** is affected by the evolution of the ferroelastic domain structure, which also influences the value of P_s.

We have calculated the P_s of the **ABB** crystal by employing one structural model on two different quantum method levels (more in the Supporting Information: Table S10 and Figure S5). Current literature shows that the estimation of the spontaneous polarization parameter in the crystals, based on theoretical methods, is generally performed with the use of the point charge method, a multipolar expansion of the charge distribution, the BP approach, nudged elastic band method. There are also a number of alternative computational approaches[39−47] being utilized in the field of P_s estimation and ferroelectric properties, especially for ferroelectric metal−organic hybrid compounds and perovskite crystals. In this

work, the BP approach at the HF and DFT-D3 method levels was used for P_s calculations. The simulations for the P_s were carried out at the same levels (RHF/def2-SVP and B3LYP-D3/def2-SVP) as for the optimization of the structure and lattice parameters. Note that BP is a quite sophisticated model because P_s is calculated directly from the electronic Hamiltonian, as derived from BP[48] theory. This model has been implemented within the CRYSTAL17 software HF framework by Dall'Olio[49] and co-workers in a study of the KNbO$_3$ perovskite crystals. The BP method discussed by us has been successfully used to calculate the P_s also for the ZnO,[50] BaTiO$_3$,[51] and NaNO$_2$[52] crystals and many other compounds.[39−47] In simple terms, it can be said that the BP approach rests on the calculation of the difference in P_s between two different geometrical configurations of the crystal by exact integration in reciprocal space. Experimentally, the P_s of a ferroelectric crystal is measured as the integral of the electric current flow through the sample during the geometry change that takes place under an applied electric field.[52] One thus measures the difference in polarization of the structures before and after the perturbation has been applied. While in the quantum mechanical approach based on the BP model, the P_s in ferroelectric materials is then evaluated through as the polarization difference between one of the two enantiomorphic structures ($\lambda = +1$ or $\lambda = -1$) and the intermediate geometric structure ($\lambda = 0$). Technically, after geometrical optimization, three subsequent runs are required. The first run is a preliminary calculation related to the $\lambda = 0$ structure, the second run is a preliminary calculation related to the $\lambda = +1$ (or $\lambda = -1$) structure, and finally the third run is performed when merging of the previous data is required. In the BP approach, a "switching parameter" λ is defined, which transforms the nuclear coordinates of the system between the two structures under investigation. In particular, we can assume $\lambda = 1$ for the ferroelectric equilibrium geometry in the absence of an applied field, $\lambda = -1$ for the ferroelectric equilibrium structure with the opposite polarization vector (see Figure 5), and ($\lambda = 0$) for the centrosymmetric, nonferroelectric structure, through which the system passes in the transformation between the two ferroelectric minima.[31]
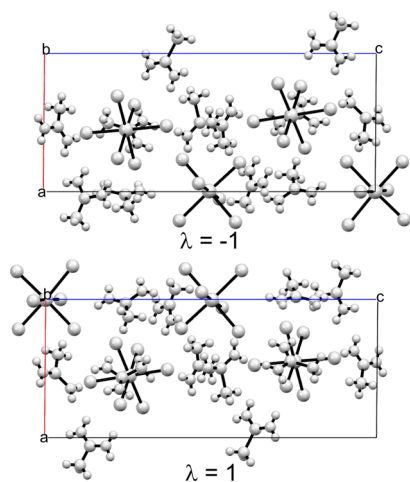

Figure 5. Crystal structure of **ABB** in the triclinic space group $P1$ along the b-axis. (a) Structure denoted as $\lambda = -1$; and (b) $\lambda = 1$ (the inverse structure of $\lambda = 1$).

The final expression for P_s within the BP theory as implemented in CRYSTAL17 software is as follows[23]

$$\Delta P_s = -\frac{i}{(2\pi)^3} \int [\langle \phi^{(\lambda=1)}(k) | \nabla_k \phi^{(\lambda=1)}(k) \rangle - \langle \phi^{(\lambda=1)}(k) | \nabla_k \phi^{(\lambda=1)}(k) \rangle] dk$$

where $\phi^{(\lambda)}$ denotes the periodic part of the crystalline orbitals.

One way to gain an additional insight into polar properties of **ABB** is to estimate its P_s using electronic structure calculations. Periodic ab initio simulations with the BP approach at the HF and DFT-D3 method levels gave P_s values of 1.69 and 1.89 μC·cm^{-2}, respectively. Both these values are larger than the experimentally determined one (0.4 μC·cm^{-2}). The differences in the experimental and computational results are probably due to sensitivity of the BP model to the structural changes. Alfredsson[52] suggested conducting simulations in the BP model even without initial geometric optimization because this approach gives better results for the HF method and structures from X-ray measurements directly. Stroppa in his work[40] drew attention to the fact how important is the structural relaxation in hybrid compounds during the P_s calculations. We believe that the differences between the experiment and the theoretical calculations may also be due to the fact that the saturated value of P_s was not reached in the dielectric measurements, and additionally the measurement of P_s was carried out on an **ABB** pellet and not on a single crystal, so that orientational averaging of the P_s vector over many crystallites takes place, effectively driving down the value of this parameter. On a different note, it should also be added that most of the P_s calculations at the DFT method level tend to overestimate slightly this value, even if compared to the experimental ones determined for single-crystal samples.

3.4. Nonlinear Optical Studies. Finally, we have also sought an additional confirmation of crystallographic symmetry of all investigated phases. With the use of TR-SHG measurements, we checked whether these phases generate second harmonic of radiation upon exposure to laser pulses of very high peak intensity because second-order (and more generally—even-order) NLO phenomena occur only in materials in which structural centrosymmetry is broken. Figure 4d displays integral intensities of the SHG signal of **ABB** for cooling (293−78 K) and heating runs (78−293 K). These results clearly demonstrate that SHG is absent in phases **I**, **II**, and **III**, while it emerges only for phase **IV**. Thermal hysteresis in the cooling−heating cycle (ca. 15 K) is apparent, corroborating the postulated discontinuous mechanism of **III−IV** PT. Nevertheless, a closer look at these plots reveals that despite a clear thermal hysteresis, the SHG signal experiences a slow onset and even a slower decay during the cooling and heating runs, respectively. Indeed, during the heating cycle, a small but non-negligible SHG response is present up to ca. 135 K, that is, the temperature point higher than those determined from DSC, pyroelectric, or dielectric studies. Taking into account the sensitivity of the employed detection setup, one can interpret that the SHG signal originates from remainders of phase **IV**, which in turn implies that discontinuous transition may be assisted by continuous reorganization. It seems that the strength of the observed effects is rather low to be of broader significance. Thus, the most important outcome of TR-SHG measurements is that phase **IV** is confirmed to be acentric and that **III−IV** PT is reversible.
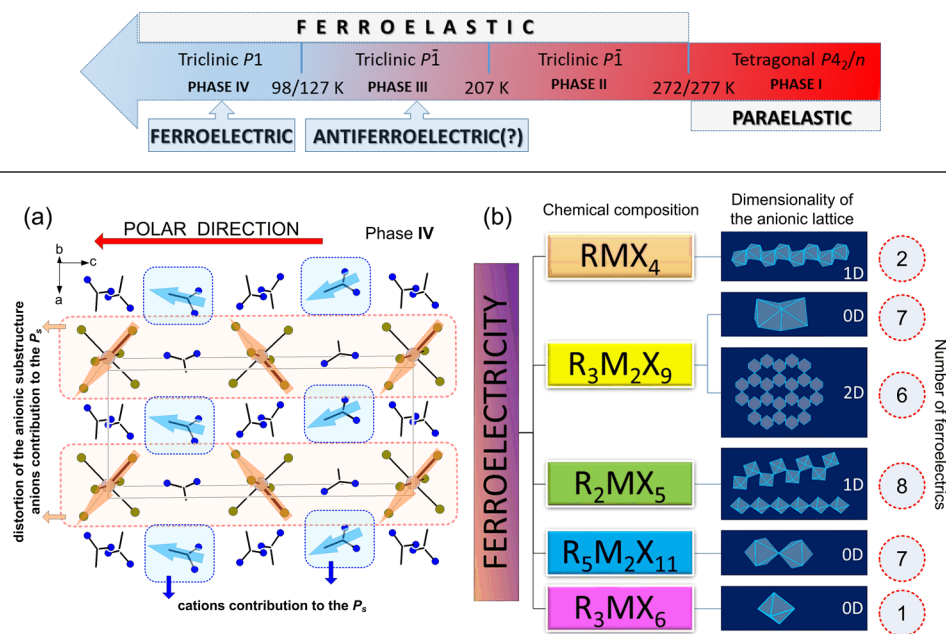
Scheme 1. Phase Diagram of ABB

Figure 6. (a) Mutual orientation of the dipole moments contributing to P_s within the cationic and anionic networks. (b) Correlation between ferroelectric properties and geometry of the inorganic part of haloantimonate(III) and halobismuthate(III) groups (only one-component organic networks of Bi(III)/Sb(III) hybrids were taken into account).

Inspection of the spectra collected during the TR-SHG experiment (Figure S6) shows that irradiation of **ABB** with 800 nm femtosecond pulses affords not only a narrow SHG signal at 400 nm for phase **IV** but also a weak broad emission (λ_{max} = 535 nm, full width at half-maximum = 85 nm at 78 K), whose presence requires an investigation. It is clear that one can see **ABB** luminescence, which must be preceded by nonlinear photon absorption, in which two or more photons can be possibly involved. Because NLO processes feature superlinear dependence of their intensity on excitation fluence, plotting the logarithm of integral area of luminescence as a function of logarithm of excitation fluence should provide a line whose slope corresponds to the number of photons participating in a given NLO process. In Figure S7 are presented the experimental spectra of the power-dependent luminescence experiment, while Figure S8 displays the corresponding $\log(I_{em}) = f(\log(P))$ plot with a least-squares linear fit. The slope of that function was found to be equal to 1.9, which indicates the two-photon absorption (i.e., the third-order NLO process) origin of the luminescence observed.

Observation of the two-photon excited luminescence calls for preliminary estimation of its efficiency. With the use of the SSTPEF technique,[53] we found that the value of two-photon brightness ($\sigma_2\varphi$, the product of two-photon absorption cross section σ_2 and quantum yield of luminescence φ) at 800 nm is ca. 5×10^{-4} GM per $(CH_3C(NH_2)_2)_3[BiBr_6]$ structural unit. This value is at least 5 orders of magnitude lower compared to those of metal−organic frameworks[54−57] or perovskites.[58−61] There are two main factors that can explain why the value of two-photon brightness for **ABB** is low. One pertains to the intrinsic structure of this material. **ABB** is composed of the isolated $[BiBr_6]^{3-}$ complex anions, which are separated from each other by a set of hydrogen bonded to their acetamidinium cations. Components contributing to **ABB** are, therefore, small, which stays in contrast with much better performing CPs and

perovskites, whose coordination nets are essentially polymeric (1D, 2D, and 3D structures). Indeed, it is a known matter that the length of electronic conjugation, and therefore the size of NLO chromophore strongly correlate with higher values of the 2PA cross section because a greater separation between charges significantly increases the polarizability of the system.[56,62] For this reason, the optical nonlinearity associated with relatively small $[BiBr_6]^{3-}$ anions is rather modest.

One also needs to consider that two-photon brightness involves a quantum yield component, which for **ABB** is assessed to be very low at room temperature (presumably below 0.1%), which is a second factor that influences the overall low value of the $\sigma_2\varphi$ product. Because measurement of such a low quantum yield value with sufficient accuracy is beyond our current measurement capabilities, we refrain from providing the σ_2 value for this material as it would be affected by a large uncertainty.

Taken together, it follows that weak two-photon performance for **ABB** is not unexpected if one considers its 0D construction. Notwithstanding this, it is the first report on the activity of a member of the halobismuthate(III) family in general.

Summarizing, $(CH_3C(NH_2)_2)_3[BiBr_6]$ (**ABB**) is the first example of the R_3MX_6 type of ferroelectric with a one-component cationic structure. **ABB** is described by a complex sequence of PTs, which have been characterized with a suite of techniques including DSC, TR-SHG, dielectric spectroscopy, and structural analysis. Based on these inputs, the following phase diagram (Scheme 1) can be proposed:

If one considers the physicochemical (ferroelectric and ferroelastic domains) properties, **ABB** is a particularly difficult object for structural analysis. The most puzzling and unexpected experimental outcome is the dielectric response in the vicinity of all PTs. Dielectric anomalies are significant only for **I → II** and **II → III** transitions and characteristic of

the antiferroelectric (at 272 K) and para-ferroelectric transformations (at 207 K), respectively.

The structural studies supported by the SHG results have proven that PT between two centrosymmetric phases **I** and **II** is a ferroic/ferroelastic one. In turn, **II → III** PT is an isostructural (nonferroic) transformation accompanied by the doubling of the unit cell. Crystallographic analysis of phase **III** reveals the antiparallel alignment of acetamidinium dipoles, suggesting the antiferrroelectric nature of this phase. Unexpectedly, ferroelectric properties have been detected below 127 K, where the dielectric response manifests itself only as an inflection of the dielectric permittivity plot, which is rather unusual as for most ferroelectrics. It is beyond doubt that phase **IV** reveals polar properties with ferroelectric ordering, confirmed by both, the pyroelectric measurement (reversibility of P_s) and the direct observation of the ferroelectric hysteresis loop. The polarization value is not large ($P_s = 0.4$ μC·cm^{-2} at 115 K), but is in the range typically found for ferroelectrics of the halobismuthate(III) subgroup.

What appears as the most unexpected result in the context of the entire sequence of PTs, is the dynamics of organic cations themselves. Structural PT at 272 K is related to the partial ordering of the acetamidinium dipoles and correlates well with the change of the entropy effect ($\Delta S = 9.4$ J·mol^{-1}·K^{-1}) indicating its "order−disorder" molecular mechanism. A change in cation dynamics through the PT at 207 K is quite subtle, thus the "displacive" mechanism is postulated. This supposition/assumption is additionally confirmed by the absence of heat anomalies in the DSC curves. Ferroelectric PT at 127 K is classified as a discontinuous one, and the mechanism of this transformation is inferred mainly from the structural data. In the case of **ABB**, ferroelectric ordering occurs as a result of changes in the position of acetamidinium cations (without reorientations) and octahedral units $[BiBr_6]^{3-}$. Therefore, the dominant mechanism is of the "displacive" type. The structural origin of P_s in phase **IV** is illustrated in Figure 6a. It is apparent that the dipole moments of cations give the largest contribution along the c-axis. By contrast, the dipole moments of the BiBr$_6$ octahedral units cancel out along the a-direction, while their c-axis projections are also the greatest.

In light of the obtained results, it is tempting to draw a concise correlation between the ferroelectric properties and the crystal structure of the anionic network in the group of haloantimonates(III) and halobismuthates(III) (see Figure 6b). Ferroelectricity is preferred only for 5 chemical stoichiometries and 7 types of anionic networks (for a total of more than 40 possible structures[6,7]). Two subclasses that are the least likely to yield ferroelectric halobismuthate(III), so far, have been the R$_3$MX$_6$- (in which only one ferroelectric has been discovered), and RMX$_4$-type compounds (two examples).[63] By contrast, the other three stoichiometries (R$_3$M$_2$X$_9$, R$_2$MX$_5$, and R$_5$M$_2$X$_{11}$) have shown a much stronger tendency to obtain materials with ferroelectric property. In this respect, the group of R$_5$M$_2$X$_{11}$ compounds particularly stands out for which all complexes obtained so far (without additional ions or solvent molecules in the crystal structure) are ferroelectrics.[6] Thus, from the viewpoint of property engineering, the R$_5$M$_2$X$_{11}$ subgroup gives the greatest chance to afford a ferroelectric structure.

The dimensionality of the anionic network appears to be a secondary factor that influences the emergence of the ferroelectric order. It is apparent that mononuclear and polynuclear (1D and 2D) anionic constructions are observed. The correlation between the dimensionality anionic network and the polarity of the crystal structure is visible if we take into account all possible anionic forms in a selected group. For example, in R$_2$MX$_5$-[64−67] or RMX$_4$-[63] type stoichiometries, despite their rich diversity of the anionic part, ferroelectricity is limited only to the 1D anionic network. The type of cation, its structure, symmetry, and size have only a limited impact on ferroelectricity generation. However, there are some exceptions. In the case of R$_3$M$_2$X$_9$ stoichiometry (2D anionic structure), cations occupy voids in 12-membered rings inside the layers $(M_2X_9^{3-})_\infty$ and thus must be of a small size (e.g., methyl-, dimethyl-, and trimethylammonium cations). In the case of R$_3$MX$_6$ complexes, no requirements as to the cation's size are imposed, thus it seems that it is only a matter of time when the next examples of ferroelectrics of this composition will be discovered.

4. CONCLUSIONS

Thus far, the ferroelectric property is evidenced for dozens of haloantimonates(III) and halobismuthates(III), the bulk of which adapted R$_2$MX$_5$, R$_3$M$_2$X$_9$, and R$_5$M$_2$X$_{11}$ stoichiometries. In this paper, we have described, for the first time, 0D halobismuthate(III) of the R$_3$MX$_6$-type compound characterized by a single-component cationic network (acetamidinium) and isolated octahedral [halobismuthate(III)] units, which appeared to be a ferroelectric at low temperatures.

The ferroelectric order in phase **IV** of **ABB** emerges as a result of the polar alignment of acetamidinium cations and octahedral complex anions $[BiBr_6]^{3-}$, for both of which the largest contribution of the dipole moment is projected along the c-axis. The mechanism of ferroelectric PT **III** ($P\bar{1}→$ **IV** ($P1$) at 98/127 K can be couched in terms of "displacive" transition for both cationic and anionic substructures. On the contrary, for the remaining PTs, that is, **II** ($P\bar{1}$) → **III** ($P\bar{1}$) at 207 K and **I** ($P4_2/n$)→ **II** ($P\bar{1}$ 272/277 K, the structural changes in the anionic substructure are of "displacive" character, whereas those in the cationic substructure are of "order−disorder" type. Such a mixed nature of PTs is consistent with the observed dielectric susceptibility spectra.

TR-SHG measurements confirmed that phase **IV** is noncentrosymmetric, and that **III−IV** PT is reversible. While performing TR-SHG measurements at 800 nm, we have also registered luminescence centered at 535 nm, and its two-photon mechanism has been postulated based on the power-dependent measurements of emission intensity. Using the SSTPEF measurement technique, we found that the value of two-photon brightness at 800 nm is fairly low (5×10^{-4} GM per $(CH_3C(NH_2)_2)_3[BiBr_6]$ structural unit), which is due to both the 0D character of **ABB** building blocks and a low quantum yield of luminescence. Regardless of the relatively weak two-photon performance of **ABB** at this wavelength, it must be stressed that this is the first report that deals with two-photon absorption properties of halobismuthates(III) in general.

We have also investigated the ferroelectric crystal structure of **ABB** with periodic HF and DFT-D3 calculations. The calculated P_s values at the optimized HF and DFT-D3 geometry and using the BP approach are 1.69 and 1.89 μC·cm^{-2}, which are overestimated relative to that of the experiment ($P_s = 0.4$ μC·cm^{-2}), although it can be attributed to the fact that experimental measurement of P_s was carried out on an **ABB** pellet and not on a single crystal. Nevertheless,

calculation of nonzero P_s supports the ferroelectric nature of phase **IV**. It can be underlined that the simulation at the HF level gives slightly better results compared to the experimental ones.

In conclusion, the acentric symmetry of **ABB** (required for polar materials) evidenced with the use of TR-SHG measurements in phase **IV** (which is in agreement with the structural results) and the observations of the (P−E) hysteresis loop and reversible pyroelectric current around 127 K indicate, without any doubt, the ferroelectric nature of the compound investigated.

■ ASSOCIATED CONTENT

ⓈI Supporting Information

The Supporting Information is available free of charge at https://pubs.acs.org/doi/10.1021/acs.chemmater.1c01266.

> Crystals of **ABB**; RT-calculated and experimental XRD diffraction patterns of **ABB**; thermograms of TGA and DTA for **ABB**; crystallographic information, data collection and refinement, geometric parameters, and H-bond geometry obtained at 295, 240, 150, and 100 K; crystal packing of **ABB** optical properties; periodic ab initio calculations; structure and atomic labeling for the **ABB** crystal after optimization; emission spectra of **ABB** under different laser powers; and log−log plot of integral intensity of **ABB** emission vs applied laser power (PDF)

■ AUTHOR INFORMATION

Corresponding Author

Anna Piecha-Bisiorek − *Faculty of Chemistry, University of Wrocław, Wrocław 50-383, Poland;* ⓞ orcid.org/0000-0002-0314-4478; Email: anna.piecha@chem.uni.wroc.pl

Authors

Klaudia Mencel − *Faculty of Chemistry, University of Wrocław, Wrocław 50-383, Poland*

Vasyl Kinzhybalo − *Institute of Low Temperature and Structure Research, Polish Academy of Sciences, Wrocław 50-422, Poland*

Ryszard Jakubas − *Faculty of Chemistry, University of Wrocław, Wrocław 50-383, Poland;* ⓞ orcid.org/0000-0002-2464-8309

Jan K. Zaręba − *Advanced Materials Engineering and Modelling Group, Faculty of Chemistry, Wrocław University of Science and Technology, Wrocław 50-370, Poland;* ⓞ orcid.org/0000-0001-6117-6876

Przemysław Szklarz − *Faculty of Chemistry, University of Wrocław, Wrocław 50-383, Poland;* ⓞ orcid.org/0000-0002-1652-4154

Piotr Durlak − *Faculty of Chemistry, University of Wrocław, Wrocław 50-383, Poland*

Marek Drozd − *Institute of Low Temperature and Structure Research, Polish Academy of Sciences, Wrocław 50-422, Poland*

Complete contact information is available at:
https://pubs.acs.org/10.1021/acs.chemmater.1c01266

Notes

The authors declare no competing financial interest.

■ REFERENCES

(1) Wu, L.-M.; Wu, X.-T.; Chen, L. Structural overview and structure−property relationships of iodoplumbate and iodobismuthate. *Coord. Chem. Rev.* **2009**, *253*, 2787−2804.

(2) Shahrokhi, S.; Gao, W.; Wang, Y.; Anandan, P. R.; Rahaman, M. Z.; Singh, S.; Wang, D.; Cazorla, C.; Yuan, G.; Liu, J.-M.; Wu, T. Emergence of Ferroelectricity in Halide Perovskites. *Small Methods* **2020**, *4*, 2000149.

(3) Saparov, B.; Mitzi, D. B. Organic-Inorganic Perovskites: Structural Versatility for Functional Materials design. *Chem. Rev.* **2016**, *116*, 4558−4596.

(4) Li, M.; Xia, Z. Recent progress of zero-dimensional luminescent metal halides. *Chem. Soc. Rev.* **2021**, *50*, 2626−2662.

(5) Jin, Z.; Zhang, Z.; Xiu, J.; Song, H.; Gatti, T.; He, Z. A critical review on bismuth and antimony halide based perovskites and their derivatives for photovoltaic applications: recent advances and challenges. *J. Mater. Chem. A* **2020**, *8*, 16166−16188.

(6) Jakubas, R.; Rok, M.; Mencel, K.; Bator, G.; Piecha-Bisiorek, A. Correlation between crystal structures and polar (ferroelectric) properties of hybrids of haloantimonates(III) and halobismuthates-(III). *Inorg. Chem. Front.* **2020**, *7*, 2107−2128.

(7) Adonin, S. A.; Sokolov, M. N.; Fedin, V. P. Polynuclear halide complexes of Bi(III): From structural diversity to the new properties. *Coord. Chem. Rev.* **2016**, *312*, 1−21.

(8) McPherson, W. G.; Meyers, E. A. Crystal structures of bismuth halide complex salts. Tris(dimethylammonium)-hexabromobismuthate(III), $[(CH_3)_2NH_2]_3BiBr_6$. *J. Phys. Chem.* **1968**, *72*, 3117−3122.

(9) Jarraya, S.; Salah, A. B.; Daoud, A.; Rothammel, W.; Burzlaff, H.; Jarraya, S. Structure of $[(C_2H_5)_2NH_2]_3BiCl_6$. *Acta Crystallogr., Sect. C: Cryst. Struct. Commun.* **1993**, *49*, 1594−1596.

(10) Lazarini, F. Structure of diethylammonium hexabromobismuthate(III). *Acta Crystallogr., Sect. C: Cryst. Struct. Commun.* **1985**, *41*, 1617−1619.

(11) Płowaś, I.; Białońska, A.; Bator, G.; Jakubas, R.; Medycki, W.; Baran, J. Tris(allylammonium) hexabromobismuthate(III) - crystal structure, phase transitions and thermal, dielectric, vibrational and ^{1}H NMR properties over a range of temperatures. *Eur. J. Inorg. Chem.* **2012**, *2012*, 636−646.

(12) Płowaś, I.; Białońska, A.; Jakubas, R.; Bator, G.; Zarychta, B.; Baran, J. Structural characterization, thermal, dielectric and vibrational properties of tris(allylammonium) hexabromoantimonate(III), $(C_3H_5NH_3)_3SbBr_6$. *Chem. Phys.* **2010**, *375*, 16−25.

(13) Wu, Z.; Liu, X.; Ji, C.; Li, L.; Wang, S.; Sun, Z.; Zhang, W.; Peng, Y.; Luo, J. Above-room-temperature switching of quadratic nonlinear optical properties in a Bi−halide organic−inorganic hybrid. *J. Mater. Chem. C* **2018**, *6*, 9532−9536.

(14) Chen, D.; Dai, F.; Hao, S.; Zhou, G.; Liu, Q.; Wolverton, C.; Zhao, J.; Xia, Z. Crystal structure and luminescence properties of lead-free metal halides $(C_6H_5CH_2NH_3)_3MBr_6$ (M = Bi and Sb). *J. Mater. Chem. C* **2020**, *8*, 7322−7329.

(15) Wang, B.; Ma, D.; Zhao, H.; Long, L.; Zheng, L. Room Temperature Lead-Free Multiaxial Inorganic−Organic Hybrid. *Inorg. Chem.* **2019**, *58*, 13953−13959.

(16) Rigaku Oxford Diffraction. *CrysAlisPro Software System*, version 1.171.38.41; Rigaku Corporation: Oxford, U.K., 2015.

(17) Sheldrick, G. M. SHELXT - Integrated space-group and crystal-structure determination. *Acta Crystallogr., Sect. A: Found. Adv.* **2015**, *71*, 3−8.

(18) Grimme, S. Semiempirical GGA-Type Density Functional Constructed with a Long-Range Dispersion Correction. *J. Comput. Chem.* **2006**, *27*, 1787−1799.

(19) Grimme, S.; Antony, J.; Ehrlich, S.; Krieg, H. A Consistent and Accurate Ab Initio Parametrization of Density Functional Dispersion Correction (DFT-D) for the 94 Elements H-Pu. *J. Chem. Phys.* **2010**, *132*, 154104.

(20) Grimme, S.; Ehrlich, S.; Goerigk, L. Effect of the Damping Function in Dispersion Corrected Density Functional Theory. *J. Comput. Chem.* **2011**, *32*, 1456−1465.

(21) Grimme, S.; Hansen, A.; Brandenburg, J. G.; Bannwarth, C. Dispersion-Corrected Mean-Field Electronic Structure Methods. *Chem. Rev.* **2016**, *116*, 5105−5154.

(22) Dovesi, R.; Erba, A.; Orlando, R.; Zicovich-Wilson, C. M.; Civalleri, B.; Maschio, L.; Rérat, M.; Casassa, S.; Baima, J.; Salustro, S.; Kirtman, B. Quantum-mechanical Condensed Matter Simulations with CRYSTAL. *WIREs Comput. Mol. Sci.* **2018**, *8*, No. e1360.

(23) Dovesi, R.; Saunders, V. R.; Roetti, C.; Orlando, R.; Zicovich-Wilson, C. M.; Pascale, F.; Civalleri, B.; Doll, K.; Harrison, N. M.; Bush, I. J.; D'Arco, P.; Llunell, M.; Causà, M.; Noël, Y.; Maschio, L.; Erba, A.; Rerat, M.; Casassa, S. *CRYSTAL17 User's Manual*; University of Torino: Torino, 2017.

(24) Becke, A. D. Density-functional thermochemistry. III. The role of exact exchange. *J. Chem. Phys.* **1993**, *98*, 5648.

(25) Lee, C.; Yang, W.; Parr, R. G. Development of the Colle-Salvetti Correlation-Energy Formula into a Functional of the Electron Density. *Phys. Rev. B* **1988**, *37*, 785−789.

(26) Vosko, S. H.; Wilk, L.; Nusair, M. Accurate Spin-Dependent Electron Liquid Correlation Energies for Local Spin Density Calculations: A Critical Analysis. *Can. J. Phys.* **1980**, *58*, 1200−1211.

(27) Monkhorst, H. J.; Pack, J. D. Special Points for Brillouin-Zone Integrations. *Phys. Rev.* **1976**, *13*, 5188−5192.

(28) Schäfer, A.; Horn, H.; Ahlrichs, R. Fully Optimized Contracted Gaussian Basis Sets for Atoms Li to Kr. *J. Chem. Phys.* **1992**, *97*, 2571−2577.

(29) Weigend, F.; Ahlrichs, R. Balanced Basis Sets of Split Valence, Triple Zeta Valence and Quadruple Zeta Valence Quality for H to Rn: Design and Assessment of Accuracy. *Phys. Chem. Chem. Phys.* **2005**, *7*, 3297−3305.

(30) Hay, P. J.; Wadt, W. R. Ab Initio Effective Core Potentials for Molecular Calculations. Potentials for K to Au Including the Outermost Core Orbitals. *J. Chem. Phys.* **1985**, *82*, 299−310.

(31) Wadt, W. R.; Hay, P. J. Ab Initio Effective Core Potentials for Molecular Calculations. Potentials for Main Group Elements Na to Bi. *J. Chem. Phys.* **1985**, *82*, 284−298.

(32) Hay, P. J.; Wadt, W. R. Ab Initio Effective Core Potentials for Molecular Calculations. Potentials for the Transition Metal Atoms Sc to Hg. *J. Chem. Phys.* **1985**, *82*, 270−283.

(33) Pascale, F.; Zicovich-Wilson, C. M.; López Gejo, F.; Civalleri, B.; Orlando, R.; Dovesi, R. The Calculation of the Vibrational Frequencies of Crystalline Compounds and Its Implementation in the CRYSTAL Code: Crystalline Compounds and the CRYSTAL Code. *J. Comput. Chem.* **2004**, *25*, 888−897.

(34) Zicovich-Wilson, C. M.; Pascale, F.; Roetti, C.; Saunders, V. R.; Orlando, R.; Dovesi, R. Calculation of the Vibration Frequencies of Alpha-Quartz: The Effect of Hamiltonian and Basis Set. *J. Comput. Chem.* **2004**, *25*, 1873−1881.

(35) Horiuchi, S.; Kagawa, F.; Hatahara, K.; Kobayashi, K.; Kumai, R.; Murakami, Y.; Tokura, Y. Above-room-temperature ferroelectricity and antiferroelectricity in benzimidazoles. *Nat. Commun.* **2012**, *3*, 1308.

(36) Tagantsev, A. K. Weak Ferroelectrics. *Ferroelectrics* **1988**, *79*, 57−60.

(37) Dvořák, V. Improper ferroelectrics. *Ferroelectrics* **1974**, *7*, 1−9.

(38) Strukov, B. A.; Levanyuk, A. P. *Ferroelectric Phenomena in Crystals*; Springer-Verlag Berlin Heidelberg: New York, 1998, Chapter 4.

(39) Zhao, W.-P.; Shi, C.; Stroppa, A.; Di Sante, D.; Cimpoesu, F.; Zhang, W. Lone-Pair-Electron-Driven Ionic Displacements in a Ferroelectric Metal-Organic Hybrid. *Inorg. Chem.* **2016**, *55*, 10337−10342.

(40) Stroppa, A.; Quarti, C.; De Angelis, F.; Picozzi, S. Ferroelectric Polarization of $CH_3NH_3PbI_3$: A Detailed Study Based on Density Functional Theory and Symmetry Mode Analysis. *J. Phys. Chem. Lett.* **2015**, *6*, 2223−2231.

(41) Kamminga, M. E.; Stroppa, A.; Picozzi, S.; Chislov, M.; Zvereva, I. A.; Baas, J.; Meetsma, A.; Blake, G. R.; Palstra, T. T. M. Polar Nature of $(CH_3NH_3)_3Bi_2I_9$ Perovskite-like Hybrids. *Inorg. Chem.* **2017**, *56*, 33−41.

(42) Hao, X. F.; Stroppa, A.; Picozzi, S.; Filippetti, A.; Franchini, C. Exceptionally Large Room-Temperature Ferroelectric Polarization in The PbNiO₃ multiferroic Nickelate: First-Principles Study. *Phys. Rev. B* **2012**, *86*, 014116.

(43) Di Sante, D.; Stroppa, A.; Jain, P.; Picozzi, S. Tuning the Ferroelectric Polarization in a Multiferroic Metal-Organic Framework. *J. Am. Chem. Soc.* **2013**, *135*, 18126−18130.

(44) Stroppa, A.; Di Sante, D.; Barone, P.; Bokdam, M.; Kresse, G.; Franchini, C.; Whangbo, M.-H.; Picozzi, S. Tunable Ferroelectric Polarization and Its Interplay with Spin-Orbit Coupling in Tin Iodide Perovskites. *Nat. Commun.* **2014**, *5*, 5900.

(45) Stroppa, A.; Jain, P.; Barone, P.; Marsman, M.; Perez-Mato, J. M.; Cheetham, A. K.; Kroto, H. W.; Picozzi, S. Electric Control of Magnetization and Interplay between Orbital Ordering and Ferroelectricity in a Multiferroic Metal-Organic Framework. *Angew. Chem., Int. Ed.* **2011**, *50*, 5847−5850.

(46) Stroppa, A.; Barone, P.; Jain, P.; Perez-Mato, J. M.; Picozzi, S. Hybrid Improper Ferroelectricity in a Multiferroic and Magneto-electric Metal-Organic Framework. *Adv. Mater.* **2013**, *25*, 2284−2290.

(47) Fan, F.-R.; Wu, H.; Nabok, D.; Hu, S.; Ren, W.; Draxl, C.; Stroppa, A. Electric-Magneto-Optical Kerr Effect in a Hybrid Organic-Inorganic Perovskite. *J. Am. Chem. Soc.* **2017**, *139*, 12883−12886.

(48) Resta, R. Macroscopic Polarization in Crystalline Dielectrics: The Geometric Phase Approach. *Rev. Mod. Phys.* **1994**, *66*, 899−915.

(49) Dall'Olio, S.; Dovesi, R.; Resta, R. Spontaneous Polarization as a Berry Phase of the Hartree-Fock Wave Function: The Case Of KNbO₃. *Phys. Rev. B* **1997**, *56*, 10105.

(50) Massidda, S.; Resta, R.; Posternak, M.; Baldereschi, A. Polarization and Dynamical Charge of ZnO within Different One-Particle Schemes. *Phys. Rev. B Condens. MAter.* **1995**, *52*, 16977−16980.

(51) Fu, L.; Yaschenko, E.; Resca, L.; Resta, R. Hartree-Fock Studies of Surface Properties Of BaTiO₃. *Phys. Rev. B* **1999**, *60*, 2697−2703.

(52) Alfredsson, M.; Hermansson, K.; Dovesi, R. Periodic Ab Initio Calculations of the Spontaneous Polarisation in Ferroelectric NaNO₂. *Phys. Chem. Chem. Phys.* **2002**, *4*, 4204−4211.

(53) Medishetty, R.; Zaręba, J. K.; Mayer, D.; Samoć, M.; Fischer, R. A. Nonlinear Optical Properties, Upconversion and Lasing in Metal-Organic Frameworks. *Chem. Soc. Rev.* **2017**, *46*, 4976−5004.

(54) Liu, M.; Quah, H. S.; Wen, S.; Li, Y.; Vittal, J. J.; Ji, W. Multiphoton Absorption and Two-Photon-Pumped Random Lasing in Crystallites of a Coordination Polymer. *J. Phys. Chem. C* **2018**, *122*, 777−781.

(55) Quah, H. S.; Nalla, V.; Zheng, K.; Lee, C. A.; Liu, X.; Vittal, J. J. Tuning Two-Photon Absorption Cross Section in Metal Organic Frameworks. *Chem. Mater.* **2017**, *29*, 7424−7430.

(56) Medishetty, R.; Nemec, L.; Nalla, V.; Henke, S.; Samoć, M.; Reuter, K.; Fischer, R. A. Multi-Photon Absorption in Metal−Organic Frameworks. *Angew. Chem., Int. Ed.* **2017**, *56*, 14743−14748.

(57) Mayer, D. C.; Manzi, A.; Medishetty, R.; Winkler, B.; Schneider, C.; Kieslich, G.; Pöthig, A.; Feldmann, J.; Fischer, R. A. Controlling Multiphoton Absorption Efficiency by Chromophore Packing in Metal−Organic Frameworks. *J. Am. Chem. Soc.* **2019**, *141*, 11594−11602.

(58) Mączka, M.; Ptak, M.; Gągor, A.; Stefańska, D.; Zaręba, J. K.; Sieradzki, A. Methylhydrazinium Lead Bromide: Noncentrosymmetric Three-Dimensional Perovskite with Exceptionally Large Framework Distortion and Green Photoluminescence. *Chem. Mater.* **2020**, *32*, 1667−1673.

(59) Chen, W.; Bhaumik, S.; Veldhuis, S.; Xing, G.; Xu, G.; Graetzel, M.; Mhaisalkar, S.; Mathews, M.; Sum, T. C. Giant five-photon absorption from multidimensional core-shell halide perovskite colloidal nanocrystals. *Nat. Commun.* **2017**, *8*, 15198.

(60) Xu, Y.; Chen, Q.; Zhang, C.; Wang, R.; Wu, H.; Zhang, X.; Xing, G.; Yu, W. W.; Wang, X.; Zhang, Y.; Xiao, M. Two-photon-pumped perovskite semiconductor nanocrystal lasers. *J. Am. Chem. Soc.* **2016**, *138*, 3761−3768.

(61) Wang, Y.; Li, X.; Zhao, X.; Xiao, L.; Zeng, H.; Sun, H. Nonlinear Absorption and Low-Threshold Multiphoton Pumped Stimulated Emission from All-Inorganic Perovskite Nanocrystals. *Nano Lett.* **2016**, *16*, 448−453.

(62) He, G. S.; Tan, L.-S.; Zheng, Q.; Prasad, P. N. Multiphoton Absorbing Materials:Molecular Designs, Characterizations and Applications. *Chem. Rev.* **2008**, *108*, 1245−1330.

(63) Gągor, A. Phase transitions in ferroelectric 4-aminopyridinium tetrachloroantimonate(III)− revisited. *Acta Crystallogr., Sect. B* **2018**, *74*, 217−225.

(64) Zhang, H.-Y.; Wei, Z.; Li, P.-F.; Tang, Y.-Y.; Liao, W.-Q.; Ye, H.-Y.; Cai, H.; Xiong, R.-G. The Narrowest Band Gap Ever Observed in Molecular Ferroelectrics: Hexane-1,6-Diammonium Pentaiodobismuth(III). *Angew. Chem., Int. Ed.* **2018**, *57*, 526−530.

(65) Piecha, A.; Białońska, A.; Jakubas, R. Novel Organic-Inorganic Hybrid Ferroelectric: Bis(Imidazolium)Pentachloroantimonate(III), $(C_3N_2H_5)_2SbCl_5$. *J. Mater. Chem.* **2012**, *22*, 333−336.

(66) Jakubas, R.; Gągor, A.; Winiarski, M. J.; Ptak, M.; Piecha-Bisiorek, A.; Ciżman, A. Ferroelectricity in Ethylammonium Bismuth-Based Organic-Inorganic Hybrid: $(C_2H_5NH_3)_2[BiBr_5]$. *Inorg. Chem.* **2020**, *59*, 3417−3427.

(67) Zhao, W.-P.; Shi, C.; Stroppa, A.; Di Sante, D.; Cimpoesu, F.; Zhang, W. Lone-Pair-Electron-Driven Ionic Displacements in a Ferroelectric Metal-Organic Hybrid. *Inorg. Chem.* **2016**, *55*, 10337−10342.

■ NOTE ADDED AFTER ASAP PUBLICATION

This paper was published on October 29, 2021, with errors in the Abstract paragraph. The corrected version was reposted November 1, 2021.